The Astronomical Journal, 140:1051–1061, 2010 October doi:10.1088/0004-6256/140/4/1051

HST AND *SPITZER* OBSERVATIONS OF THE HD 207129 DEBRIS RING

John E. Krist[1], Karl R. Stapelfeldt[1], Geoffrey Bryden[1,2], George H. Rieke[3], K. Y. L. Su[3], Christine C. Chen[4], Charles A. Beichman[2], Dean C. Hines[5], Luisa M. Rebull[6], Angelle Tanner[7], David E. Trilling[8], Mark Clampin[9], and András Gáspár[3]

[1] Jet Propulsion Laboratory, California Institute of Technology, 4800 Oak Grove Drive, Pasadena, CA 91109, USA
[2] NASA Exoplanet Science Institute, California Institute of Technology, 770 S. Wilson Ave., Pasadena, CA 91125, USA
[3] Steward Observatory, University of Arizona, 933 N. Cherry Ave., Tucson, AZ 85721, USA
[4] Space Telescope Science Institute, 3700 San Martin Drive, Baltimore, MD 21218, USA
[5] Space Science Institute, 4750 Walnut St. Suite 205, Boulder, CO 80301, USA
[6] Spitzer Science Center, Mail Stop 220-6, California Institute of Technology, Pasadena, CA 91125, USA
[7] Georgia State University, Department of Physics and Astronomy, One Park Place, Atlanta, GA 30316, USA
[8] Department of Physics and Astronomy, Northern Arizona University, Box 6010, Flagstaff, AZ 86011, USA
[9] NASA Goddard Space Flight Center, Greenbelt, MD 20771, USA
Received 2010 April 26; accepted 2010 August 14; published 2010 September 9

ABSTRACT

A debris ring around the star HD 207129 (G0V; $d = 16.0$ pc) has been imaged in scattered visible light with the ACS coronagraph on the *Hubble Space Telescope* (*HST*) and in thermal emission using MIPS on the *Spitzer Space Telescope* at $\lambda = 70\ \mu$m (resolved) and 160 μm (unresolved). *Spitzer* IRS ($\lambda = 7$–$35\ \mu$m) and MIPS ($\lambda = 55$–$90\ \mu$m) spectrographs measured disk emission at $\lambda > 28\ \mu$m. In the *HST* image the disk appears as a ∼30 AU wide ring with a mean radius of ∼163 AU and is inclined by 60° from pole-on. At 70 μm, it appears partially resolved and is elongated in the same direction and with nearly the same size as seen with *HST* in scattered light. At 0.6 μm, the ring shows no significant brightness asymmetry, implying little or no forward scattering by its constituent dust. With a mean surface brightness of $V = 23.7$ mag arcsec^{-2}, it is the faintest disk imaged to date in scattered light. We model the ring's infrared spectral energy distribution (SED) using a dust population fixed at the location where *HST* detects the scattered light. The observed SED is well fit by this model, with no requirement for additional unseen debris zones. The firm constraint on the dust radial distance breaks the usual grain size–distance degeneracy that exists in modeling of spatially unresolved disks, and allows us to infer a minimum grain size of ∼2.8 μm and a dust size distribution power-law spectral index of −3.9. An albedo of ∼5% is inferred from the integrated brightness of the ring in scattered light. The low-albedo and isotropic scattering properties are inconsistent with Mie theory for astronomical silicates with the inferred grain size and show the need for further modeling using more complex grain shapes or compositions. Brightness limits are also presented for six other main-sequence stars with strong *Spitzer* excess around which *HST* detects no circumstellar nebulosity (HD 10472, HD 21997, HD 38206, HD 82943, HD 113556, and HD 138965).

Key words: circumstellar matter – stars: individual (HD 207129, HD 10472, HD 21997, HD 38206, HD 82943, HD 113556, HD 138965, HD 211415)

Online-only material: color figures

1. INTRODUCTION

Circumstellar debris disks are created by the collisions or disruptions of solid bodies (asteroids, comets, planets) that generate clouds of small dust grains. Radiation pressure, Poynting–Robertson drag, and stellar winds can remove these particles on timescales much less than the age of the star. Thus, seeing a debris disk means that either a major collision of large objects has recently occurred in the system or that the dust is continually replenished through collisions within a reservoir of smaller bodies. Either way, these disks signify the presence of some kind of planetary system. They also offer the chance to view a system of planetesimals for signs of unseen planets or very low mass companions by way of central clearings, gaps, localized clumps, or spiral arms caused by planetary perturbations on the disk structure.

An increasing number of debris disks are being resolved, especially around solar-type stars. Infrared measurements from the InfraRed Astronomical Satellite (*IRAS*), *Infrared Space Observatory* (*ISO*), and *Spitzer* space telescopes have been used to identify disk candidates based on far-infrared flux densities well in excess of those expected for stellar photospheres. A few have been resolved in long-wavelength emission with *Spitzer* and submillimeter radio telescopes. Such disks, like those around β Pictoris (Heap et al. 2000) or Fomalhaut (Kalas et al. 2005), have low optical depths that make them difficult to image in scattered light relative to the glare created by the stars and telescope. High contrast imaging techniques are required, including a coronagraph to suppress the diffraction pattern of the star and point-spread function (PSF) subtraction to reduce the residual instrumentally scattered light. While ground-based observations use these methods, the lack of wavefront stability due to atmospheric turbulence, even after correction by adaptive optics, precludes them from detecting all but the brightest debris disks. This is largely due to image instabilities that lead to significant PSF subtraction residuals. The *Hubble Space Telescope* (*HST*) avoids this problem entirely and provides a highly stable wavefront, making it the premier tool for debris disk imaging. The coronagraph on the Advanced Camera for Surveys (ACS) provided the highest contrast imaging capability on *HST* (Krist 2004) until its failure in early 2007.

By showing the location of orbiting planetesimals and, in some cases, by identifying disk asymmetries caused by individual planets, debris disk images probe the architecture

of planetary systems around other stars. For the most direct comparison with the solar system, debris disks around mature solar-type stars are of particular interest. We consider here the nearby Sun-like star HD 207129 (HR 8323, HIP 107649, GJ 838, IRAS 21450-4732; $V = 5.58$), a G0V star at a *Hipparcos*-measured distance of 16.0 pc (van Leeuwen 2007). Walker & Wolstencroft (1988) noted that HD 207129 had a small *IRAS* 60 μm excess while Habing et al. (1996) measured 60 and 90 μm *ISO* excesses, indications of circumstellar material, most likely a disk. Jourdain de Muizon et al. (1999) obtained additional *ISO* observations over $\lambda = 2.5$–180 μm and verified that there was no significant excess below 25 μm. This indicates the lack of circumstellar material near the star and thus a central clearing in the disk. They suggested that a substellar companion interior to the clearing may be required to maintain the hole as Poynting–Robertson drag would cause dust to migrate toward the star and fill it on short timescales. Sheret et al. (2004) were unable to detect the disk at $\lambda = 450$ and 850 μm using SCUBA. Using the submillimeter non-detections as upper limits and combining the *IRAS* and *ISO* results, they derived a disk radius of 260 ± 50 AU. However, Zuckerman & Song (2004) derived a 35 AU orbital radius by assuming that large dust grains emit as a blackbody at $T \sim 50$ K. This highlights a problem with determining disk sizes from unresolved photometric measurements: degeneracies exist among the grain size, emissivity, temperature, and distance from the star, and thus the size scale of the disk is uncertain. For example, see the analysis of the HD 12039 disk by Hines et al. (2006). By directly measuring the location of the dust, resolved images of the disk can break these degeneracies and allow reliable grain properties to be derived.

In an effort to increase the number of resolved debris disks, we utilized the ACS coronagraph to image disk candidate stars selected based on their infrared excesses measured with the *IRAS*, *ISO*, and *Spitzer* space telescopes. Most disk candidates with higher optical depths (implied by $L_{\rm dust}/L_\star \gtrsim 5 \times 10^{-4}$) have previously been imaged by *HST* and ground-based telescopes. To date, the lowest optical depth disk seen in scattered light is Fomalhaut's (Kalas et al. 2005), which has $L_{\rm dust}/L_\star = 8 \times 10^{-5}$. We chose eight targets previously unobserved by *HST* having $L_{\rm dust}/L_\star = 1$–7×10^{-4}, including HD 207129. We report here the detection of a disk around that star and, as an appendix, non-detections around six of the other targets (the detection of the disk around HD 10647 is discussed in K. R. Stapelfeldt et al. 2010, in preparation).

2. OBSERVATIONS AND DATA PROCESSING

2.1. HST ACS Observations

HD 207129 was observed on 2006 May 3 with the coronagraph in the ACS High Resolution Camera (HRC; $\sim$0.″025 pixel^{-1}) in *HST* program 10539. Two observation sequences were executed, each consisting of a 0.1 s exposure in the narrowband filter F502N for automated acquisition and centering of the star behind the coronagraphic occulting spot, and a 100 s exposure and four 520 s exposures in F606W with the star centered behind the 1.″8 diameter occulter. At the beginning of the first sequence, two 0.3 s direct (non-coronagraphic) exposures in filter F606W (ACS wide *V* band) were taken to provide unsaturated images for accurate stellar photometry. Each sequence required one orbit, and the two sequences were executed in consecutive orbits. Between them, the telescope was rolled 20.°0 about the line of sight to provide additional discrimination between real objects and instrumental artifacts (instrumental artifacts appear stationary on the detector while the sky image rotates).

While the coronagraph suppresses the diffraction pattern created by the telescope, it does not reduce the scattering by optical surface errors that create a halo of light around the star. This halo is typically subtracted using an image of another isolated star observed in the same manner. This is practical because the *HST* PSF is generally stable over time (compared to ground-based telescopes). The G3V star HD 211415 ($V = 5.33$) was observed in the orbit following the two HD 207129 orbits to provide a reference PSF. It was selected because it has a similar color to HD 207129 and is nearby in the sky. Unfortunately, our images showed the presence of a companion star located 2.″2 away at P.A. = 43.°2 and 4.5 mag fainter.[10] In the coronagraphic images, the companion is highly saturated, rendering these images unsuitable for use for PSF subtraction. As will be described later, an alternative subtraction method was used instead.

The ACS images were calibrated by the *HST* pipeline. Multiple long exposures were combined and cosmic rays were rejected. Image count rates were converted to standard *V* magnitudes using the zero point obtained from the SYNPHOT synthetic photometry program based on a stellar spectrum of similar type to HD 207129.

2.2. HST ACS PSF Subtraction

As previously noted, the designated PSF subtraction reference star, HD 211415, was a binary. To replace it, 10 similarly observed alternative reference stars were collected from our program and the *HST* Archive. Each was subtracted from the combined long-exposure HD 207129 images. This was done by iteratively shifting the reference image via interpolation, adjusting its normalization, and subtracting it from the science image until the residual instrumental halo was minimized by eye. None of these subtractions indicated the presence of any circumstellar material above the level of the residuals, and they are therefore of no further use. Using these reference stars was not optimal because the telescope focus and the coronagraphic occulter position are known to vary over time, and this selection of reference stars was not matched in color with HD 207129 as HD 211415 had been. These differences between the PSF reference stars and the science target can cause significant subtraction residuals.

The only viable alternative processing technique was to use the image of HD 207129 taken at one orientation to subtract the starlight from the image taken at the other and vice versa, a process called roll subtraction. Because the images were taken close in time, this reduces the effects of time-dependent changes in the telescope, and there is no color mismatch. However, any extended disk could subtract part of itself in the other orientation, thus this method is best suited to nebulosity that is confined along a preferred axis through the star, such as an edge-on disk (a symmetric face-on disk would completely subtract itself, for example).

A roll-subtracted image contains a positive image of a disk and a negative one rotated by an angle equal to the difference between the telescope orientations. Ideally, these two would be combined to form a single, positive image, but that is difficult to

[10] Jasinta et al. (1995) also report this object with separation of 4.″96 at P.A. 37.°8, and identical brightness relative to the primary star. Given HD 211415's large proper motion of 771 mas year^{-1} at P.A. 124.°8 (Perryman et al. 1997), this must be a bound companion star in a nearly edge-on orbit with semimajor axis $\sim$100 AU.

do after subtraction. Instead of directly subtracting images from the two orientations and then trying to combine the results, an iterative technique can be used that solves for those portions of the two unsubtracted images that appear static on the detector (i.e., the PSF) and those that appear to rotate as the telescope rolls (i.e., the sky, including any disk). Such a method was used to subtract the *HST* Space Telescope Imaging Spectrograph images of β Pictoris (Heap et al. 2000), whose edge-on disk is well suited for this.

The procedure begins with an initial estimate of the static (PSF) component, which is the average of the unsubtracted (raw) images (it is assumed that the PSF is largely stable between the two observations). At this point, any rotating (sky) features from each orientation in this static image are now half of their original intensities compared to the total static component. This estimate of the static component is then subtracted from each raw image, creating the initial sky estimate at each orientation. One of the sky frames is then rotated to the orientation of the other, and the two are then averaged. This new sky frame is then subtracted from each raw frame (after rotation), and the result is averaged, creating a new static estimate. In each subsequent iteration, the residual sky features in the estimated static (PSF) component are reduced in intensity by a factor of two. This process is repeated until the sky frame does not visibly change.

The above method was applied to the long-exposure HD 207129 data. Before doing so, the images from the two roll angles were shifted via interpolation to a common center, to remove small residual pointing offsets between the two. The subtraction procedure was then run for eight iterations. The result revealed a very faint, inclined ring centered on the star. To improve the signal, the original images were downsampled to 0.″1 resolution using 4×4 rebinning and the subtraction process repeated with improved results (Figure 1).

To verify that the subtraction algorithm can produce a reliable result, we have tested our detection procedure on a simulated disk image combined with an observed ACS coronagraphic PSF. For the star we used ACS images of HD 82943, which was also observed in our program with sequences similar to those for HD 207129. A noiseless model of the HD 207129 ring with twice its surface brightness relative to the star was added at each orientation and then processed. The results shown in Figure 2 indicate that this method can reliably extract such a disk from these data. Another experiment with the disk model having a filled interior but otherwise the same inclination and size showed that the extracted disk image also had a filled interior, so the inner clearing in the real disk is not caused by self-subtraction.

It is unlikely that this disk would have been detected by subtracting a reference star image, as we had originally intended with HD 211415. There is always a PSF mismatch due to color differences when a reference PSF is used. This disk is so faint that it might have been detected only by using roll subtraction and avoiding such color mismatches.

2.3. Spitzer Photometry and Spectroscopy

The Multiband Imaging Photometer for *Spitzer* (MIPS) instrument was used to image HD 207129 at 24 μm on 2004 October 13 as a part of GTO program 41 (Beichman et al. 2005). One cycle of the standard photometry dither pattern was executed, producing a data set with 16×3 s exposures. Mosaics with 2.″45 square pixels from the Spitzer Science Center (SSC) post-BCD pipeline version 14.4 (providing enhanced processing beyond the basic calibrated data) were used for our analysis. Photometry in a 13″ aperture yielded a total flux density of 164 ± 2 mJy, using the aperture corrections of Engelbracht et al. (2007). This value is consistent with the one obtained by Trilling et al. (2008) from the same data set.

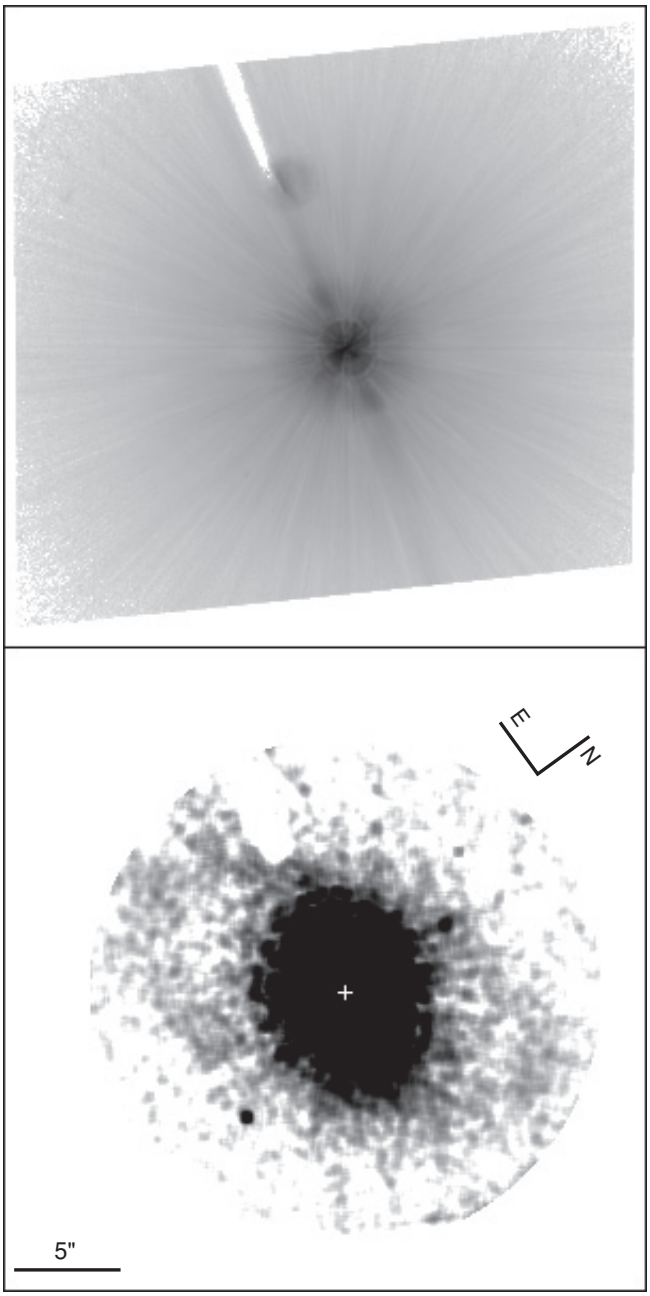

Figure 1. ACS F606W coronagraphic observations of HD 207129. Each frame is 30.″2 on a side. Top: coronagraphic image from the first orientation prior to PSF subtraction. Shadows of the occulting finger and larger occulting spot are seen toward the upper left corner. The diagonal streak stretching from the upper left to lower right is instrumentally scattered light. This image is displayed with logarithmic intensity scaling. Bottom: image of the HD 207129 ring after applying the iterative roll subtraction method described in the text to the exposures taken at each orientation. The images were rebinned to 0.″1 sampling prior to processing, and the result was additionally smoothed using a median filter. This image is displayed with a quarter-root intensity scaling with a much lower maximum value compared to the top image.

MIPS 70 μm default scale imaging of HD 207129 was performed by Bryden et al. (unpublished), and clearly showed the source to be extended. Follow-up imaging using the MIPS 70 μm fine scale channel was carried out on 2006 November 3 as a part of GO program 31057. Five cycles of the

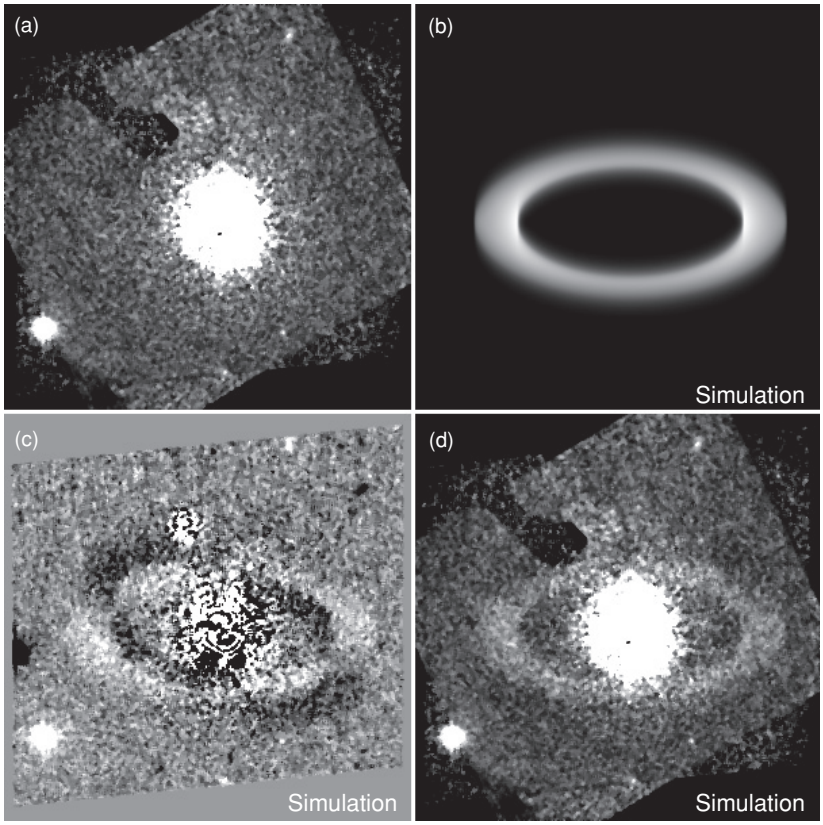

Figure 2. Experimental results of applying the roll subtraction algorithm to ACS F606W coronagraphic images of HD 82943 taken at two orientations separated by 25°. Each frame is 30.″2 on a side. (a) Result of the application of the algorithm prior to adding a disk model to the images. The residuals near the center are due to PSF mismatches between the two orientations. (b) Model disk that approximately matches the observed HD 207129 ring. This is added to each HD 82943 image (with a 25° orientation offset in the second image) without noise and with twice the surface brightness of the HD 207129 ring. (c) Direct subtraction of the image from the second orientation from that from the first (with disk models added). Positive and negative images of the ring and background objects are seen. (d) Application of the roll subtraction algorithm to the ring-added images. The resulting ring image appears cleaner than that for HD 207129 because of the increased surface brightness and lack of shot noise in the model.

small-field photometry dither pattern and 10 s exposures were made at each of four cluster target positions spaced on a square grid of 16.″22 (3.16 pixel) spacing. This observing strategy provides enhanced subpixel sampling to enable PSF subtraction and deconvolution, and an effective exposure time of $5 \times 4 \times 84 = 1680$ s on the source. The data were processed using the MIPS Data Analysis Tool (DAT; Gordon et al. 2005) version 3.10, with final output mosaics made on a grid with 2.″62 pixels. The source appears clearly extended, as expected from the prior default scale images. Structure in the sky background around the source complicates measurement of the source flux. Photometry of the fine scale data using a 15 pixel square aperture, with an aperture correction derived from STinyTIM PSF simulations (Krist 2006), finds 70 μm flux densities ranging from 244 to 317 mJy, depending on where the background is chosen. The midpoint of these values is consistent with the flux density of 289 mJy reported for the default scale data by Trilling et al. (2008), and is much brighter than the stellar photospheric emission. However, reprocessing of the default scale data using the most recent MIPS instrument team pipeline produces images with a smoother background and fewer artifacts. Photometry in those mosaics (4.″925 pixel^{-1}) using a 16 pixel aperture yields a flux density of 369 ± 26 mJy. As HD 207129 is a red source, a color correction factor of 1.12 (assuming a color temperature of 50 K) must be applied to yield a final 70 μm flux density of 413 ± 29 mJy.

MIPS 160 μm observations were carried out on 2007 June 4 as a part of GO program 30157. Three cycles of 10 s exposures were made at each of nine cluster target positions. The target spacings provided offsets of 0″ and ± 36″ (2.5 pixels) along the short axis of the 2 × 20 pixel array, and 0″, 72″, and 140″ along the long axis to provide a larger area for background measurements. The total exposure time on the source was $3 \times 9 \times 64 = 1728$ s. Data processing was again with the MIPS DAT version 3.10, with the final product being a 130 × 58 pixel mosaic at 4″ pixel scale. The short-wavelength spectral leak is present adjacent to the image of HD 207129, with intensity about half of the true source brightness. This spurious source was removed by aligning and subtracting an image of τ Ceti, an object for which MIPS detects only the spectral leak at 160 μm. Photometry of the leak-subtracted image is also complicated by variable background levels near the source. Depending on the sky aperture placement, background-subtracted flux densities in a 16 pixel square aperture range from 218 to 283 mJy, with a 12% overall calibration uncertainty. We therefore adopt a compromise value of 250 ± 40 mJy for the source at 160 μm. This is somewhat larger than the value derived by Tanner et al. (2009) from a different MIPS data set, and is about 30% less than the value obtained from ISOPHOT observations by Jourdain de Muizon et al. (1999)—probably because of source confusion in the large *ISO* beam (see Section 3.2).

MIPS spectral energy distribution (SED) mode observations of HD 207129 were performed on 2007 October 27 as a part of GTO program 30156. This observing mode produces $R \sim 15$–25 spectroscopy over the wavelength range from 55 to 90 μm. The 120″ × 20″ slit was oriented along P.A. 229°,

or roughly perpendicular to the disk major axis determined by Bryden et al. (unpublished). Fifteen cycles of 10 s exposures were used, giving a total integration time of 944 s. By chopping 1′ off-source, a background spectrum was obtained and subtracted from the source spectrum. Reduction of the spectral images was done using the MIPS DAT version 3.10, which produced a mosaic with 44 4.″9 pixels in the spatial direction and 65 pixels in the spectral direction. This was then boxcar-smoothed over five adjacent rows to improve the measured signal to noise ratio. To extract the spectrum, the signal in five columns centered on the peak emission was summed along each row of the SED mosaic. The resulting spectrum in instrumental units was converted to physical units by reducing and extracting a MIPS spectrum of the calibration star Canopus (F0 II) in the same way. The Canopus spectrum was re-normalized to give a flux density of 3.11 Jy at 70 μm, and corrected for the spectral response function by assuming Canopus has a Rayleigh–Jeans spectral slope in the far-IR. The flux normalization and spectral response function derived from Canopus were then applied to the MIPS spectrum of HD 207129, and the resultant spectrum was further smoothed over adjacent wavelength bins. This reduction process assumes a point-source slit loss correction; a revised slit loss correction becomes necessary when fitting spatially extended source models to these data (Section 4).

Spitzer's InfraRed Spectrograph (IRS) was used to observe HD 207129 on 2007 June 10 as part of GO program 20065. Exposure times of 2 × 6 s, 3 × 14 s, and 5 × 30 s were employed for the Short-Low1 (SL1; 7–14 μm), Long-Low2 (LL2; 14–21 μm), and Long-Low1 (LL1; 20–28 μm) spectral modules, respectively. The data were processed by the standard (SSC) pipeline version 16.1. Spectra were obtained for each order at two positions along the slit and extracted using the SSC SPICE (Spitzer IRS Custom Extraction) software package. The resulting flux is an average of these two nod positions, while the error bars are calculated from the difference between them. The entrance slit for the SL spectrograph is just 3.″7 wide, resulting in potential loss of some incoming flux depending on how well centered the target is within the slit. The LL slit width of 10.″6 is much less prone to pointing-related slit loss. This is confirmed by comparison with the MIPS photometry, where the IRS flux density at 24 μm (165 mJy) is in excellent agreement with the aforementioned MIPS 24 μm value, and well within the nominal ∼2% calibration uncertainty for MIPS at 24 μm (Engelbracht et al. 2007). Due to slit loss, however, the SL data had to be scaled upward by a constant factor of 1.08 in order to properly overlap with the LL data. Following this scaling, data from the three spectral orders were spliced together by simple removal of the low signal-to-noise ratio edges of each order, resulting in a final wavelength coverage from 7.6 to 35 μm. Here also, a point-source slit loss correction is assumed and must be revised when modeling an extended source (Section 4).

3. RESULTS

3.1. HST ACS

The ACS image reveals that the HD 207129 disk is a ring inclined 60° ± 3° from pole-on with its major axis along P.A. = 127° ± 3°, as measured by visually fitting ellipses. The annulus is ∼1.″9 (∼30 AU) wide with a mean radius of ∼10.″2 (163 AU). The ansae have a surface brightness of $V = 23.7 \pm 0.3$ mag arcsec^{-2}, which is 22× less than that of the unsubtracted coronagraphic stellar PSF at those locations. This makes the HD 207129 ring the faintest extrasolar circumstellar disk to have been imaged in scattered light (the Fomalhaut ring surface brightness of $V = 22$ mag arcsec^{-2} makes it the faintest disk relative to the brightness of its star; Kalas et al. 2005). The similarity of the nebula surface brightness on opposite sides of the ring major axis indicates a dust phase function with low scattering anisotropy (see below), and thus provides no clear indication whether the N or S side of the ring is foreground to the star. Overall the ring structure appears azimuthally smooth; noise and subtraction residuals make it impossible to discern how uniform it is on small scales. No strong constraint can be given on the presence of material interior to the ring: the shot noise remaining after PSF subtraction increases steeply inward (see the Appendix), negating the effect of increased stellar illumination at smaller radial distances.

Three objects are detected near the ring. A point source is seen 7.″50 from HD 207129 at P.A. = 196°, projected just outside the ring edge. It has a brightness of $V = 22.8 \pm 0.3$ (the uncertainty is largely due to the non-uniform background of PSF subtraction residuals). A more diffuse source that is likely to be a background galaxy is 5.″6 away at P.A. = 359°. Another galaxy is 14.″9 from the star at P.A. = 115°. An inspection of Digital Sky Survey images shows that there are a moderate amount of both stars and galaxies in the region, so lacking any color or proper motion information to indicate otherwise, it is possible that the point source is a background star and is not associated with HD 207129. Further observations are needed to test for companionship via common proper motion.

3.2. Spitzer Imaging and Spectroscopy

Mid and far-infrared images of HD 207129 and its surrounding field are shown in Figure 3. At 24 μm, the star appears as an unresolved point source. To check for faint extended emission, a 24 μm image of the reference star HD 217382 (which lacks any infrared excess) was aligned with that of HD 207129 and subtracted. The results show no significant extended emission from the disk at 24 μm.

At 70 μm the source is clearly extended, with the fine scale source well-fit by an elliptical Gaussian with FWHM 25.″1 × 17.″7 and major axis along P.A. 123°. To retrieve the intrinsic source size from these values we must make comparisons to images of standard stars. The bright reference stars Altair, Sirius, and Procyon have a median elliptical Gaussian source size of 16.″1 × 15.″3 in MIPS 70 μm fine scale images. However, these sources lack IR excess, have a Rayleigh–Jeans slope across the 70 μm bandpass, and thus are significantly bluer than HD 207129. They will thus appear slightly smaller than an unresolved source with strong excess, and this difference can be important to size estimates when the source extension is less than the telescope beamwidth. By integrating the product of different spectral slopes with the MIPS 70 μm filter bandpass, we estimate that telescope diffraction should cause a flat spectrum source to appear 3.1% larger than a naked photosphere. Using this correction, quadrature subtraction of the beamsize from the data results in an intrinsic source size of 18.″8 ± 0.″8 (300 ± 13 AU) along its major axis and 8.″1 ± 0.″6 (130 ± 10 AU) along its minor axis. The inclination and position angles implied for the ring are consistent with the *HST* results, with the ring marginally smaller at 70 μm than seen in scattered light.

At 160 μm the measured source size is 42.″4 × 34.″0 extended along P.A. 137°. While this result is suggestive of a source elongated at the same P.A. as seen at 70 μm and with *HST*, it must be interpreted with caution. Similarly constructed 160 μm mosaics of other targets consistently show point sources

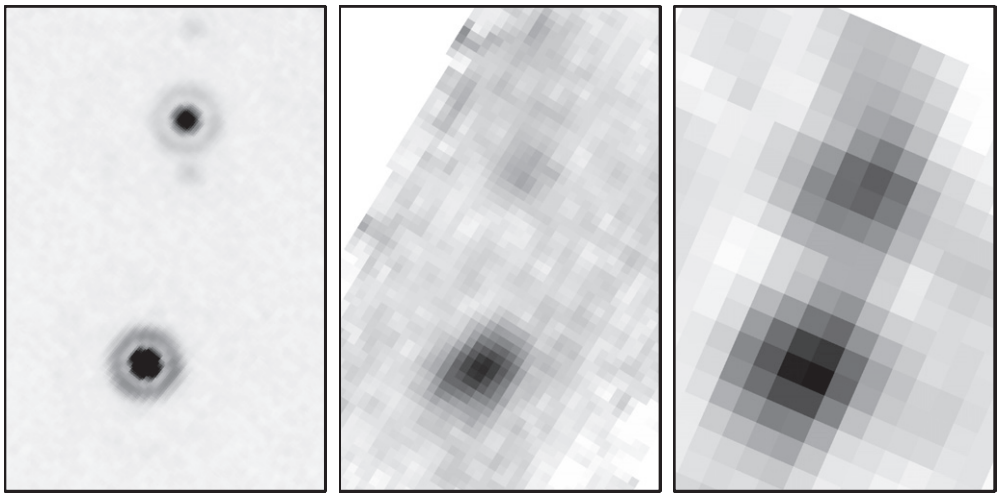

Figure 3. *Spitzer* MIPS images of HD 207129 (lower center), from left to right at 24, 70, and 160 μm, respectively. The field of view is 100″ × 150″, with N up and E to the left. The 24 μm image is shown in log stretch, while the 70 and 160 μm images are in linear stretch. Only the 70 μm fine scale image is shown. The spectral leak has been subtracted from the 160 μm image shown. The star CD-47 13929 is seen 75″ N of HD 207129 at 24 μm. A very red background object is located 59″ N of HD 207129.

instrumentally elongated by ∼20% in the direction of MIPS scan mirror motion. In the case of the HD 207129, 160 μm observation, this instrumental axis is aligned within 20° of the observed source extension. Furthermore, imperfections in subtraction of the 160 μm spectral leak could create systematic errors in the source profile that will confuse our ability to measure small deviations from an unresolved source. An intrinsic FWHM of the 160 μm source thus cannot be reliably determined, and we can only exclude source diameters larger than about half the beamsize (20″/320 AU).

The SED of HD 207129 is plotted in Figure 4. Excess emission first becomes evident near 28 μm, rises steeply to a plateau between 60–90 μm, and then falls off toward longer wavelengths. The wavy pattern in the MIPS SED spectrum between 50 and 90 μm is an artifact of the spectral extraction process. At 160 μm, MIPS measures a flux density 70% of the *ISO* values reported by Jourdain de Muizon et al. (1999). This is likely due to source confusion in the large-beam *ISO* measurements, which included both the star and the (presumably extragalactic background) source about 1′ to the north. The new 870 μm continuum detection of the source by Nilsson et al. (2010) is shown. At 24 μm, the measured flux density is comparable to the photospheric emission value of 160 mJy derived from a Rayleigh–Jeans extrapolation of the IRS SL measurements. Trilling et al. (2008) had reported a 24 μm excess for HD 207129, based on a photospheric flux density estimate 15% smaller than our value. It now appears that Trilling's photosphere flux density estimate was adversely affected by saturated 2MASS photometry, and should be superseded by the value given here from the IRS SL spectrum. Thus the star has no excess emission at 24 μm.

4. A COMBINED IMAGE AND SED MODEL

The detection of the ring in scattered light provides a new opportunity to understand the overall properties of this debris system. Previous work based only on the SED inferred a large disk outer radius of 500–1000 AU, large disk inner hole of 200 AU, and particle sizes ranging from 1 to 200 μm (Jourdain de Muizon et al. 1999). Our *HST* and *Spitzer* images show a much smaller and narrower ring. Given this new information on the spatial scale of the system, and the improved far-infrared

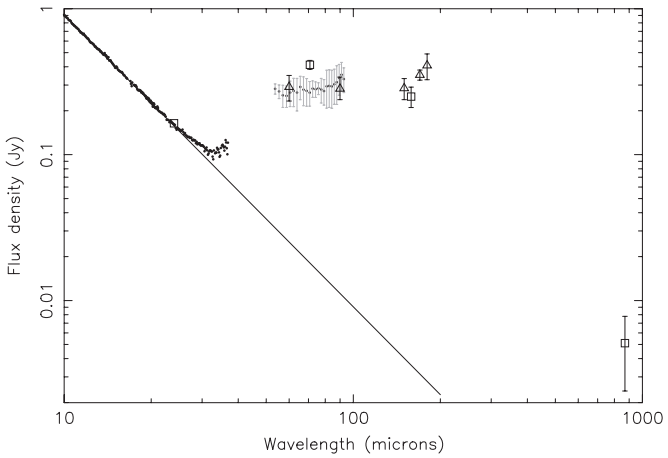

Figure 4. Spectral energy distribution of HD 207129. Individual data points show the IRS and MIPS SED results, while the three MIPS photometry points are plotted as open squares. *ISO* measurements appear as open triangles. The solid line shows a Rayleigh–Jeans extrapolation of the stellar photosphere emission based on the IRS data near $\lambda = 10\,\mu$m. The MIPS–SED spectrum shown here includes a slit loss correction for a point source; therefore, it is low compared to the 70 μm photometry which includes extended emission. The 870 micron point is from Nilsson et al. (2010).

photometry and spectroscopy provided by *Spitzer*, an updated model analysis of the disk is now called for.

We begin with the simple assumption that the disk emission originates in a single radial zone specified by inner and outer radius, a radial power-law surface density, Gaussian vertical scale height and radial flaring exponent, and astronomical silicate grains whose wavelength-dependent emissivities are calculated from Mie theory with the optical constants of Laor & Draine (1993). Dust thermal emission is calculated assuming local thermal equilibrium with a 1.2 $L_\odot$ star (Bryden et al. 2006) for each of the grain sizes considered in the distribution between minimum and maximum radii $a_{\rm min}$ and $a_{\rm max}$. The grain size distribution is at first assumed to follow an $a^{-3.5}$ power law appropriate to a collisional cascade (Dohnanyi 1969), but other slopes are considered. Initial values for the ring geometrical parameters are taken from the *HST* image (Section 3.1). Model thermal images are then calculated for this dust distribution

on a 1″ spatial grid for 31 wavelengths spanning 10–850 μm. The total flux in these 31 channels is compared to the SED of the infrared excess emission, while appropriate subsets of model images are combined to synthesize broadband images as observed by the MIPS 24, 70, and 160 μm cameras. Model images within the 7–35 μm region sampled by the IRS data, and within the 55–90 μm region sampled by the MIPS SED mode, are convolved with the instrumental PSF and windowed by synthetic entrance slits appropriate to the instrument and slit position angle used in the *Spitzer* observation. A model scattered light image is calculated for the same dust density distribution on a spatial grid of 1″, with the dust albedo and phase function asymmetry parameter as additional inputs. Isotropic scattering is assumed.

Comparison of model spectra to the observations requires careful consideration of slit losses. The IRS and MIPS SED data are normally calibrated with slit loss corrections appropriate to a point source, with the goal of making their flux calibration consistent with large-aperture MIPS 24 and 70 μm photometry. For a spatially extended source such as the ring of HD 207129, a point-source slit loss correction is no longer appropriate for calibration of these spectra. The true slit loss correction will depend in detail on the specific source brightness distribution, which is model dependent. Rather than derive slit loss corrections and recalibrate the spectral data for each possible model SED, we choose to compare model spectra that have suffered uncorrected slit losses to a version of the *Spitzer* data that has had its point-source slit loss correction removed. Slit loss correction factors for the IRS SL and LL data were derived using the IRS CUBISM software v1.6 (Smith et al. 2007). MIPS SED slit loss correction factors were calculated by windowing STinyTIM PSFs (Krist 2006) through synthetic entrance slits at six wavelengths spanning 50–90 μm and interpolating as needed for intermediate wavelengths. A nominal slit width of 20″ was assumed.

We seek a global model that can reproduce the infrared photometry, spectroscopy, resolved source size at 70 μm, and the scattered light brightness seen in the *HST* image. With its superior spatial resolution, the ACS coronagraphic image fixes the radial location of the dust within the 148–178 AU region, as well as the ring inclination and position angle. An optimal model for the *Spitzer* data was sought manually by varying the normal optical depth and the minimum/maximum silicate grain radii $a_{\rm min}$ and $a_{\rm max}$. Our initial guess for $a_{\rm min}$ was 0.6 μm, the geometric blowout size for grains with density 2.5 gm cm^{-3}, stellar luminosity of 1.2 $L_{\odot}$, and stellar mass of 1.1 $M_{\odot}$ (Equation (A19) of Plavchan et al. 2009; values from http://nsted.ipac.caltech.edu).

An initial solution was found for model parameters with $a_{\rm min}$ of 1.4 μm, $a_{\rm max}$ of 400 μm, and a normal geometrical optical depth of 0.013 for grains with radius $a_{\rm min}$ at r = 163 AU. The model reproduces the observed FWHM of the source at 70 μm; the slightly smaller source diameter at 70 μm, relative to the ring seen in scattered light, can be understood by the warmest emission being concentrated at the ring inner edge. Integrating over the grain size distribution, and assuming a mean grain density of 2.5 gm cm^{-3}, the total dust surface density is 4×10^{-6} gm cm^{-2} at $r = 160$ AU and the dust mass in the model integrated over the full spatial extent of the ring is 0.07 lunar masses. A sharp ring inner edge provides a good match to the steeply rising excess emission beyond 30 μm, and the lack of scattered light emission inside radii of 148 AU. We found that the nominal −3.5 power-law slope caused the model to overpredict the 160 μm flux density relative to 70 μm. By steepening the grain size distribution to a −3.9 power law, an adequate fit is obtained. This change strongly suppresses the submillimeter flux from the model; to compensate, a larger value of $a_{\rm max} = 700$ μm is adopted. A slope $\leqslant -3.7$ is compatible with the measurements within the errors. This slope is preferred by recent numerical simulations of the equilibrium grain size distribution when material strength effects are considered (A. Gáspár 2010, in preparation).

While this model provides a good fit to the available photometry and the spectrophotometry measured through the IRS and MIPS SED slits, it fails in its predicted scattered light brightness. According to Mie theory, astronomical silicate grains larger than 1 μm radius should have an albedo $\omega = Q_{\rm scat}/(Q_{\rm abs} + Q_{\rm scat})$ of ∼55% in the optical and near-infrared. This value was assumed in the thermal equilibrium calculations intrinsic to the SED model. For this value, and integrating over the grain size distribution of our preferred model, the model ring is much brighter in scattered light than the *HST*-measured surface brightness on the ring ansae.

The fraction of the stellar luminosity scattered by the grains, relative to the total luminosity incident on the grains, provides a wavelength-averaged albedo that can be estimated from the available data:

$$\langle\omega\rangle = F_{\rm scat}/(F_{\rm scat} + F_{\rm emit}) \quad (1)$$

where $F_{\rm scat}$ is the fractional scattered light luminosity of the disk (relative to direct starlight), and $F_{\rm emit}$ is the fractional infrared luminosity of the disk $= 1.4\times10^{-4}$ from the *Spitzer* data. $F_{\rm scat}$ is estimated from the *HST* images by renormalizing our scattered light model image of the ring so that its surface brightness on the ansa matches the observed value, and then adding up the total scattered light in the model ring structure. The result finds that $F_{\rm scat} \approx 7.6 \times 10^{-6}$. To the extent that this value, measured at 0.6 μm, is representative of the fraction of scattered to direct starlight averaged over the wavelengths that produce significant stellar heating of the grains, the mean albedo of the dust particles would be $\langle\omega\rangle \approx 5.1\%$. Simple Mie theory grains are thus not consistent with the combined suite of observations for HD 207129.

When the SED modeling is repeated using this reduced albedo, but retaining the original Mie values for $Q_{\rm scat}$, a very similar model is obtained where the only required change is that $a_{\rm min}$ increases to 2.8 μm. The higher grain emissivity causes larger grains to come to the same equilibrium temperature as the smaller, more reflective grains initially assumed. In making this adjustment, we have retained the emissive properties of astronomical silicate grains but modified their reflectivity: essentially painting the grains black. Porous dust grains might account for this results, as they are thought to have lower albedoes (Hage & Greenberg 1990) and larger blowout sizes (Saija et al. 2003) in comparison to solid grains made from the same material.

The best matching SED model with the modified grain albedo is shown in Figure 5. Future work will be needed to assess what combination of grain properties and scattering theory can provide a self-consistent solution to the emissivity and albedo values we found necessary to fit the optical and infrared properties of the HD 207129 ring.

5. DISCUSSION

HD 207129 joins the small but growing list of stars that have resolved debris disks imaged in scattered light, which

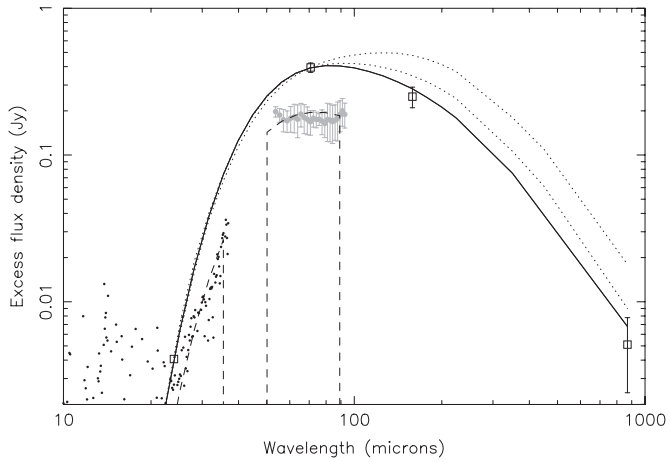

Figure 5. Infrared excess of HD 207129 (points), compared to our preferred disk model (solid line) and the disk model windowed by the IRS and MIPS SED slits (dashed lines). The stellar photosphere emission has been removed using a Rayleigh–Jeans slope normalized to the IRS SL data. Relative to Figure 4, the excess flux densities measured in the IRS and MIPS SED spectra have been reprocessed to remove the point-source slit loss correction. The effects of changing the dust size distribution slope from −3.5 (upper dotted curve) to −3.7 (lower dotted curve) to −3.9 (solid curve) are shown. All of the models have the modified albedo.

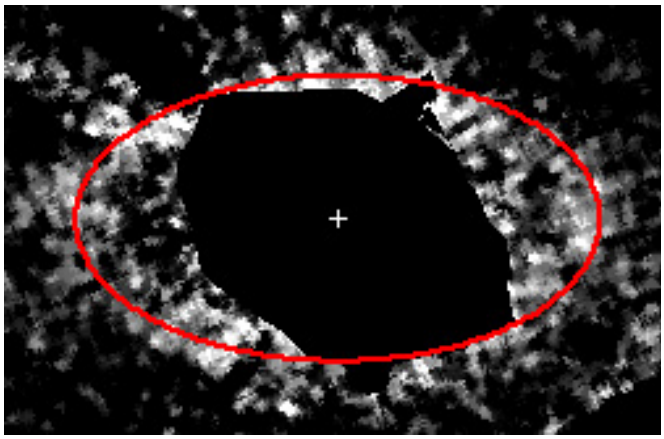

Figure 6. HD 207129 ring ACS image with an ellipse superposed centered on the star (marked by the cross) and having a semimajor axis of 10″. No large offset of the ring relative to the star, like that seen for Fomalhaut, is seen that would suggest a significant planetary perturber.

(A color version of this figure is available in the online journal.)

as of the time of writing number nearly 20.[11] The ring-like appearance of its disk is similar to those of HR 4796 and Fomalhaut, whose central cleared zones suggest the presence of low mass substellar companions that tidally remove dust. The most prominent example of this behavior is the Fomalhaut ring (Quillen 2006; Chiang et al. 2009), which is eccentric, has a sharp inner edge, and for which the predicted companion has been subsequently imaged (Kalas et al. 2008). The low definition of the HD 207129 ring makes it difficult to measure its properties precisely. A sharp ring inner edge is indicated by the steeply rising excess emission beyond 30 μm, and is consistent with the absence of scattered light inside a radius of 150 AU. A planet sculpting the ring may lie just inside this radius, but no field objects are seen there in our coronagraphic images. The point source projected near the S outer edge of the ring could be relevant to the ring dynamics, if it was found to be a comoving member of the system. Its brightness in F606W would correspond to $a > 20\ M_{\rm Jupiter}$ brown dwarf, according to the spectral evolutionary model of Burrows et al. (2003).

To constrain a possible offset of the ring center from the star, we visually overlaid ellipses on the ring image (Figure 6) to fit for the ring center. We find that any offset of the star from the ring center must be smaller than 0.″4 and 0.″2 along the ring minor and major axes (respectively). The corresponding upper limit to any ring eccentricity is 0.08, for the case where the line of apsides would be projected farthest from the plane of the sky.

The low signal of the HD 207129 ring in the ACS images limits our measurement accuracy and thus only rough characteristics can be derived. The lack of a significant difference in brightness in the near and far sides of the ring indicates nearly isotropic scattering. Based on comparisons to our approximate ring models (Figure 7), we constrain the asymmetry parameter, g, of the Henyey–Greenstein scattering phase function to be <0.1. This low level of forward scattering is only matched by the disk of HD 92945 (D. A. Golimowski et al. 2011, in preparation). Other debris disks, like Fomalhaut (Kalas et al. 2005), HD 141569a (Clampin et al. 2003), AU Mic (Krist et al. 2005), and HD 107146 (Ardila et al. 2004) have more forward scattering ($g > 0.15$).

The nearly isotropic scattering in the ring conflicts with any assumption of spherical particles that scatter according to Mie theory. Our combined scattering+SED modeling indicates that the minimum grain size is ∼2.8 μm. Spherical 2.8 μm particles are predicted to be strongly forward scattering for wavelengths less than the grain size ($g \approx 0.8$ at $\lambda = 0.6$ μm). If such grains were present in the HD 207129 ring, then the foreground portion of the ring should appear much brighter than the ansae or back side. This effect is not seen in the *HST* images. In Mie theory, astronomical silicate grains with characteristic radius <0.05 μm would be needed to match this result, and would appear much warmer than the ∼44 K temperature that characterizes the SED. Combined with the low derived albedo, this result points to non-spherical, possibly porous or coated grains.

Previous estimates for the age of HD 207129 have ranged from as little as 30–40 Myr (Zuckerman et al. 2001) to as high as 4.4–8.3 Gyr (Lachaume et al. 1999; Trilling et al. 2008). The very young age estimate has been withdrawn, but an age as young as 600 Myrs is still suggested (Song et al. 2003, 2004). A recent recalibration of the dependence of chromospheric activity on stellar age suggests an age of 2.1 Gyrs (Mamajek & Hillenbrand 2008) based on its Ca II emission strength of $\log R'_{\rm HK} = -4.8$ (Henry et al. 1996). This is consistent with an age estimated based on Li abundances measured by Soderblom (1985). However, the X-ray luminosity of this source (1.5×10^{29} erg s^{-1}, based on the *ROSAT* source counts and a nominal spectrum) is considerably larger than typical for members of the NGC 752 cluster at age 1.9 Gyr (Giardino et al. 2008). An age of 1 Gyr is plausible.

The detection of this disk in scattered light is rather fortuitous. As measured by its 10^{-4} fractional emission luminosity, it is among the lowest dust content disks to have been imaged. If the material were more widely distributed radially around the star (such as in the case of β Pic) instead of concentrated in a ring, its surface brightness would be significantly reduced. In addition, if the star were 30 pc away rather than ∼15 pc, the disk would appear half as far from the star and would be lost in the greater glare and PSF subtraction residuals that exist there. The star is also bright enough ($V = 5.6$) for

[11] See http://circumstellardisks.org for an up to date census of resolved disks.

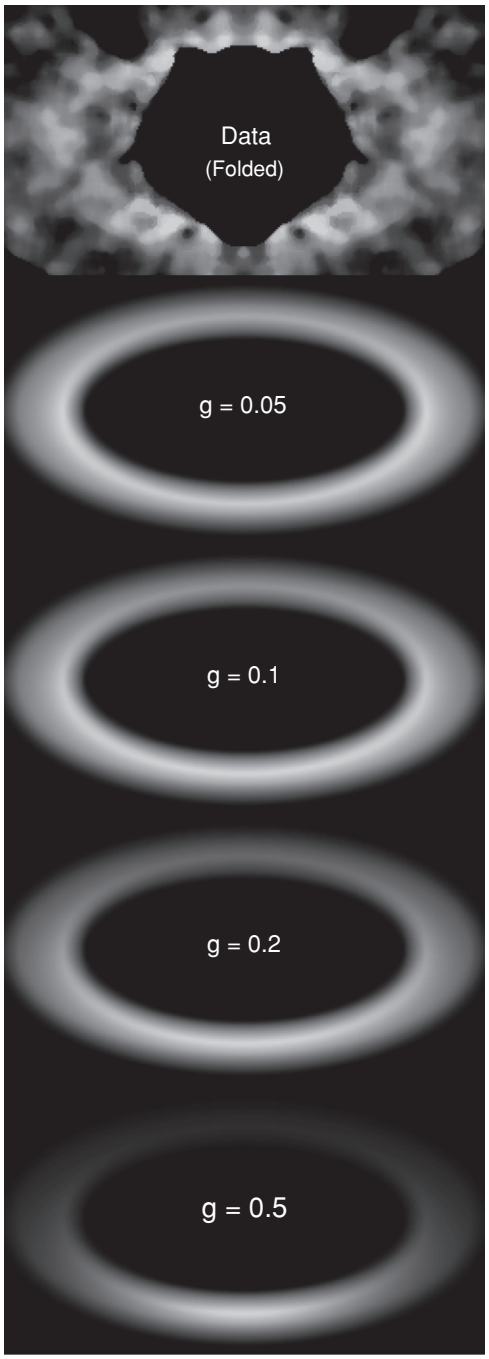

Figure 7. At the top is the ACS image of the HD 207129 ring. To improve the signal, a copy of the original image was flipped about the star (left semimajor axis onto right semimajor axis), the two added together, and then smoothed. Below it are three-dimensional scattered light disk models with different values of the Henyey–Greenstein phase term, g. These demonstrate by comparison that the actual ring does not have significantly forward scattering (large g) grains. All images are displayed with linear intensity stretches between their minimum and maximum values.

sufficient scattered light to be detected. These same conditions apply for Fomalhaut ($d = 7.7$ pc, $V = 1.2$), which has a somewhat lower fractional excess ($\sim 8 \times 10^{-5}$). These examples highlight the considerations required when optimizing a target list for coronagraphic observations, especially given the limited observing resources on *HST* in both time and coronagraphic performance. Targets that are too far away and have too low an excess are poor candidates with little chance of a detection.

6. CONCLUSIONS

HST coronagraphic images detect the debris disk of HD 207129 as a narrow ring with radius 160 AU, significantly smaller than previous estimates based only on analysis of the source SED. The ring size and orientation are comparable to that inferred from resolved MIPS images of the source at 70 μm. This ring is among the faintest circumstellar features ever detected with *HST*, and was only reliably extracted from stellar PSF artifacts through the use of a roll self-subtraction technique.

Given the new definition of the system geometry, we fit a model to the *Spitzer* images and spectrophotometry. We find that the observed emission is consistent with material in the single radial zone where *HST* detects scattered light, and with dust grains ranging from 2.8 μm to at least 500 μm radius. However, the almost isotropic scattering properties and low albedo of the ring particles are not consistent with simple Mie theory estimates for silicate grain composition. The narrowness of the ring, its apparently sharp inner edge, and large central cleared region are similar to the Fomalhaut system, and suggest that deep near-IR imaging searches for substellar/planetary companions might be profitable in the HD 207129 system. Further observations with *Herschel* could refine the ring emission properties for a more detailed comparison to the *HST* images, while far-IR spectroscopy might provide some better indication of the dust composition.

We thank Paul Smith (University of Arizona) for his assistance with the MIPS SED data, and Karl Misselt and Viktor Zubko for calculating optical properties of grains at large size parameters. This work was supported by *Hubble Space Telescope* General Observer Grant 10539 to the Jet Propulsion Laboratory, California Institute of Technology and by the *Spitzer* Project Science Office at JPL. Funding from both was provided by the National Aeronautics and Space Administration. The *Spitzer Space Telescope* is operated by the Jet Propulsion Laboratory, California Institute of Technology, under NASA contract 1407.

APPENDIX

In addition to HD 207129, we observed seven other debris disks selected from *Spitzer* results to have fractional infrared luminosities $\geqslant 10^{-4}$. The disk of HD 10647 (distance = 17 pc) was detected and will be reported in K. R. Stapelfeldt et al. (2010, in preparation). The other six are listed in Table 1. None of these showed scattered light at the contrast and inner angle limit ($r \approx 1\farcs0$) of the ACS coronagraph. The non-detections provide new constraints on the disk properties as these observations represent the highest contrast observations to date of those targets.

All of the candidates were observed using sequences similar to those used for HD 207129, with small variations in exposure lengths and roll separations (20°–30°) as imposed by *HST* pointing constraints. Reference stars (specified in Table 1) were observed and their images subtracted as described for HD 207129. Each subtracted image contained a faint, symmetric halo around the star caused by PSF mismatches that were largely due to color differences but also time-dependent changes in the optical system. These halos could hide potential, otherwise-detectable face-on disks. No disks were detected using reference PSF subtractions. The iterative roll subtraction method was also applied to these targets, using 4×4 rebinned data, and no disks were detected.

To estimate extended source detection limits in the roll-subtracted images, $1'' \times 1''$ uniform intensity squares were added

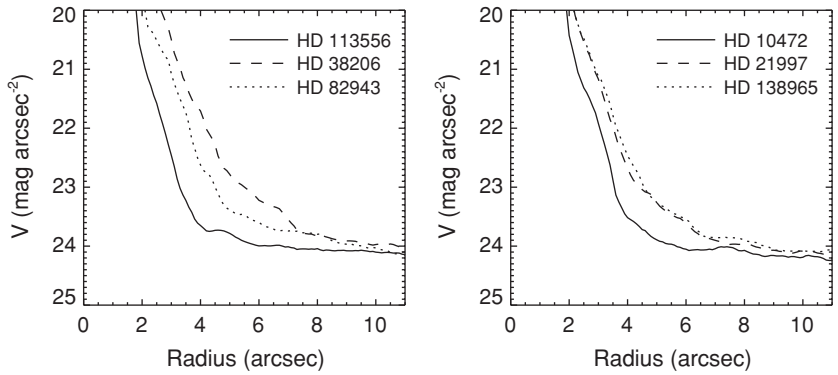

Figure 8. Lower limits for the reliable visual detection of a 1″ × 1″ uniform intensity square around six stars for which no disks were detected.

Table 1
Debris Disk Non-detections in *HST* Program 10539

Target	Spectral Type	V (mag)	Distance (pc)	PSF Star	Observation Date	$L_{\rm dust}/L_{\star}$ ($\times 10^{-4}$)	*Spitzer* Reference
HD 10472	F2IV/V	7.6	67	HD 12894	2005 Oct 2	7	Rebull et al. 2008
HD 21997	A3IV/V	6.4	74	HD 15427	2006 Aug 12	5	Moór et al. 2006
HD 38206	A0V	5.7	69	HD 41695	2005 Nov 1	1	Su et al. 2006
HD 82943	G0	6.5	27	HD 84117	2005 Nov 23	1	Trilling et al. 2008
HD 113556	F2V	8.2	102	HD 101727	2006 Apr 13	7	Chen et al. 2005
HD 138965	A1V	6.4	77	HD 167468	2006 Jun 1	4	Morales et al. 2009

to the two unsubtracted images of HD 82943 at various locations with appropriate orientations. These were then 4 × 4 rebinned and processed with the roll subtraction algorithm. This process was continually repeated with adjustments made to the squares' brightnesses until they appeared at their minimum robust visual detection limit. The local root-mean-squared (rms) noise was measured in the same locations as the squares but in a square-free roll subtraction. It appeared that the detection limit (in flux per pixel) for the squares was approximately equal to 1.2× the local rms per pixel noise.

For each roll-subtracted image of each target, the mean azimuthal rms was computed at each radius centered on the star in the subtracted image. In this calculation, care was taken to avoid background objects such as galaxies and field stars. These rms noise curves versus radius were then converted to detection limits using the factor of 1.2 and were then converted to V magnitude surface brightnesses. The resulting curves in Figure 8 show that read noise and perhaps sky background noise at large angles set the detection limit to about 24 mag arcsec^{-2} regardless of star brightness. The detection limit increases closer to the star where subtraction residuals, which scale with star brightness, dominate.

While the detection limits presented here are expressed in absolute units, what really matters is the limiting brightness relative to the star, given that a debris disk is optically thin and scales in brightness with its star. A relative detection limit can be converted to a maximum allowed optical depth along the line of sight. This can then be used to place constraints on some disk properties, but only if a number other properties are known as multiple parameters can affect line-of-sight optical depth: dust density, albedo, disk height, inclination, degree of forward scattering, etc. The maximum allowed optical depth (τ) times the albedo (ω) at a given radius r (arcseconds) from the star is $\omega\tau = 4\pi r^2 \times 10^{-0.4({\rm SB}-V_{\rm star})}$, where SB is the detection limit in mag arcsec^{-2} and $V_{\rm star}$ is the magnitude of the star. Note that ω includes any possible brightening of one side of a disk due to asymmetric scattering. In general, $\omega\tau$ at 3″ is about (1–2) × 10^{-4} for these stars.

Possible reasons for not detecting a disk around one of these six candidates include a low grain albedo (which would render the disk faint), a small disk angular radius (which could leave the system hidden behind the occulting spot), or a face-on orientation (which would make the disk more difficult to distinguish from PSF residuals).

Among the targets surveyed, HD 38206's low $v \sin i$ (Royer et al. 2002) may indicate that the disk is projected nearly face-on (assuming the disk is coplanar with the star's equator) and thus has a low line-of-sight optical depth. HD 82943, the nearest of the six disk non-detections, has two radial velocity planets near 1 AU (Mayor et al. 2004). Ground-based adaptive optics imaging also failed to detect this disk in scattered light (Schütz et al. 2004); due the highly stable PSF of *HST*, our limiting surface brightness (Figure 8) is 5 mag better. This system is comparable to HD 207129 in terms of its stellar type, V magnitude, fractional disk luminosity, and infrared excess SED. A ring comparable to that of HD 207129 would have an apparent radius of 6″ in the HD 82943 system. Scattered light residuals at this radius are only a bit worse than at 10″ where the HD 207129 ring was detected, so the non-detection of HD 82943's disk in scattered light indicates different grain properties, a more face-on orientation, or a greater radial width of the emitting region. The disk of the most distant candidate, HD 113556, would go undetected if its outer radius was less than 150 AU. Based on the observed excess ratio between 24 and 70 μm, all eight disks we studied have a characteristic blackbody temperature between 60 and 80 K.

The most prominent difference between the detected and undetected disks is their proximity: $d < 20$ pc for the two detected systems. This suggests that a disk's angular extent may be the most important property for detectability with *HST*, both to avoid blockage by the occulting spot and the higher PSF subtraction residuals found closer to the star. Future

detection surveys for debris disks in scattered light should focus on the nearest (suitably bright) stars with strong infrared excess.

REFERENCES

Ardila, D. R., et al. 2004, ApJ, 617, L147
Beichman, C. A., et al. 2005, ApJ, 622, 1160
Bryden, G., et al. 2006, ApJ, 636, 1098
Burrows, A., Sudarsky, D., & Lunine, J. I. 2003, ApJ, 596, 587
Chen, C. H., Jura, M., Gordon, K. D., & Blaylock, M. 2005, ApJ, 623, 493
Chiang, E., Kite, E., Kalas, P., Graham, J. R., & Clampin, M. 2009, ApJ, 693, 734
Clampin, M., et al. 2003, AJ, 126, 385
Dohnanyi, J. W. 1969, J. Geophys. Res., 74, 2531
Engelbracht, C. W., et al. 2007, PASP, 119, 994
Giardino, G., Pillitteri, I., Favata, F., & Micela, G. 2008, A&A, 490, 113
Gordon, K. D., et al. 2005, PASP, 117, 503
Habing, H. J., et al. 1996, A&A, 315, L233
Hage, J. I., & Greenberg, J. M. 1990, ApJ, 361, 251
Heap, S. R., et al. 2000, ApJ, 539, 435
Henry, T. J., Soderblom, D. R., Donahue, R. A., & Baliunas, S. L. 1996, AJ, 111, 439
Hines, D. C., et al. 2006, ApJ, 638, 1070
Jasinta, D. M. D., Raharto, M., & Soegiartini, E. 1995, A&AS, 114, 487
Jourdain de Muizon, M., et al. 1999, A&A, 350, 875
Kalas, P., Graham, J. R., & Clampin, M. 2005, Nature, 435, 1067
Kalas, P., et al. 2008, Science, 322, 1345
Krist, J. E. 2004, Proc. SPIE, 5487, 1284
Krist, J. E. 2006, Tiny Tim for Spitzer Version 2.0, http://ssc.spitzer.caltech.edu/archanaly/contributed/stinytim/index.html
Krist, J. E., et al. 2005, AJ, 129, 1008
Lachaume, R., Dominik, C., Lanz, T., & Habing, H. J. 1999, A&A, 348, 897
Laor, A., & Draine, B. T. 1993, ApJ, 402, 441
Lu, N., et al. 2008, PASP, 120, 328
Mamajek, E. E., & Hillenbrand, L. A. 2008, ApJ, 687, 1264
Mayor, M., Udry, S., Naef, D., Pepe, F., Queloz, D., Santos, N. C., & Burnet, M. 2004, A&A, 415, 391
Moór, A., Ábrahám, P., Derekas, A., Kiss, C., Kiss, L. L., Apai, D., Grady, C., & Henning, T. 2006, ApJ, 644, 525
Morales, F. Y., et al. 2009, ApJ, 699, 1067
Nilsson, R., et al. 2010, A&A, 518, A40
Perryman, M. A. C., et al. 1997, A&A, 323, L49
Plavchan, P., Werner, M. W., Chen, C. H., Stapelfeldt, K. R., Su, K. Y. L., Stauffer, J. R., & Song, I. 2009, ApJ, 698, 1068
Quillen, A. C. 2006, MNRAS, 372, L14
Rebull, L. M., et al. 2008, ApJ, 681, 1484
Royer, G., Grenier, S., Baylac, M.-O., Gomez, A. E., & Zorec, J. 2002, A&A, 393, 897
Saija, R., Iatì, M. A., Giusto, A., Borghese, F., Denti, P., Aiello, S., & Cecchi-Pestellini, C. 2003, MNRAS, 341, 1239
Schütz, O., Böhnhardt, H., Pantin, E., Sterzik, M., Els, S., Hahn, J., & Henning, T. 2004, A&A, 424, 613
Sheret, I., Dent, W. R. F., & Wyatt, M. C. 2004, MNRAS, 348, 1282
Smith, J. D. T., et al. 2007, PASP, 119, 1133
Soderblom, D. R. 1985, PASP, 97, 54
Song, I., Zuckerman, B., & Bessell, M. S. 2003, ApJ, 599, 342
Song, I., Zuckerman, B., & Bessell, M. S. 2004, ApJ, 614, L125
Su, K. Y. L., et al. 2006, ApJ, 653, 675
Tanner, A., Beichman, C., Bryden, G., Lisse, C., & Lawler, S. 2009, ApJ, 704, 109
Trilling, D. E., et al. 2008, ApJ, 674, 1086
van Leeuwen, F. 2007, A&A, 474, 653
Walker, H. J., & Wolstencroft, R. D. 1988, PASP, 100, 1509
Zuckerman, B., Song, I., & Webb, R. A. 2001, ApJ, 559, 388
Zuckerman, B., & Webb, R. A. 2000, ApJ, 535, 959
Zuckerman, B., & Song, I. 2004, ApJ, 603, 738